Relevant material characterization for load prediction in incremental forming

A. Abdelkefi, Dominique Guines, Lionel Leotoing, S. Thuillier

Relevant material characterization for load prediction in incremental forming

A. Abdelkefi[1], D. Guines[1], L. Léotoing[1], S. Thuillier[2*]

[1] Université de Rennes, INSA Rennes, LGCGM, CS70839, 35708 Rennes Cedex 7, France

[2] Univ. Bretagne Sud, UMR CNRS 6027, IRDL, F-56100 Lorient, France

[*] corresponding author: Sandrine Thuillier, sandrine.thuillier@univ-ubs.fr

Abstract

Robotic incremental sheet forming has arisen a recent industrial interest, as a more flexible and cost-effective solution to the process using rigid computer numerical control (CNC) machines. However, the numerical prediction of the forming loads and final geometry coupled to an elastic modeling of the robot is essential to optimize the robot trajectory and thus to ensure the geometrical accuracy of the final part. Within this context, the aim of this study is to investigate the accuracy of the load prediction in the case of a single point incremental forming process of a commercially pure (CP) titanium alloy sheet. The mechanical behavior is characterized at room temperature under two strain states, i.e., uniaxial and biaxial tension, and a truncated cone of the same material is obtained by single point incremental forming. A 3D cell records all the components of the applied load during the forming and the part is laser scanned at the end of the process, though still clamped along the outer edge. A numerical model of the process is developed assuming some symmetries to reduce the computational time. The influence of the hardening law, either identified from the uniaxial or biaxial tensile tests, on the forming load prediction is investigated, with a focus on the strain path during single point incremental forming.

Keywords

Single point incremental forming; titanium alloy; mechanical behavior; uniaxial and biaxial tension; numerical model; forming load.

1. Introduction

The single point incremental forming (SPIF) process is a flexible technology for customized products and prototyping, well adapted for small batch. During this process, the sheet is clamped and locally deformed by a moving simple tool. Initially, the forming operation was performed with a conventional computer numerical control (CNC) machine. Recently,

industrial robots have also been used to reduce tooling manufacturing costs and to improve production versatility. However, they present a high compliance and the contact forces developed during the process between the tool and the sheet can lead to a deflection of the robot structure and then to tool path errors [1]. An approach coupling a finite element (FE) model of the process with the elastic modeling of the robot structure is developed, to improve the accuracy of the robotized process. The numerical model gives a prediction of the forming loads, which are then used as input to the elastic model of the robot [2]. The quality and reliability of such a procedure highly depends on the accuracy of the predicted forces during the forming process. However, though FE models based on isotropic hardening, clamped boundary conditions, rigid tool and frictionless contact between the sheet and the tool, are usually suitable to predict correctly the final shape of the part, e.g. [3] and [4] when springback is considered, they usually give an overestimation of the forming load [5]. This inaccuracy is explained by three main factors: the finite element type that influences, in particular, the taking account of transverse shear, the boundary conditions modeling, especially for the clamping system and finally, the description of the mechanical behavior of the sheet metal and mainly the hardening model as well as the yield criterion.

Several authors [6-11] show that the prediction of the forces in SPIF depends on the type of the finite element, like 3D or shell element, and on the modeling of either the whole geometry or a reduced one with symmetry conditions. Sena et al. [12] have compared different 3D element types (8-nodes brick element with incompatible mode, reduced or full integration, respectively C3D8I, C3D8R and C3D8 for Abaqus software, with 4 elements in the thickness) in the case of a simple groove in the center of the blank made with SPIF process. It is shown that C3D8I elements give a predictive force close to the one measured experimentally. Two formulations are also compared, respectively a 4-node, stress/displacement shell element with reduced integration and a large-strain formulation (S4R) and a 8-node linear brick element with full integration and incompatible modes (C3D8I), using four elements in the thickness [13]. The difference between both types of elements is the ability of the brick model to represent the through thickness shear stress components. Finally, the authors suggested to use a mixed brick-shell elements model, that shows a good potential to predict the forces in comparison with the shell model. Several methods are suggested to save computational time, like sub-structuring the part into purely elastic and elasto-plastic areas [11]. Another approach is to introduce symmetry conditions leading to a reduced model [6]. These authors show that a 45° model reduces considerably the computation time (divided by 70) but underestimates the predicted forces by 10% compared to the full model. An alternative solution consists of using a 90° model, that

gives a forming load close to the one obtained with the full model [6-14], and allows a better representation of the material anisotropy.

The boundary conditions are also a predominant factor in the prediction of forming loads. The clamping system of the outer edge is usually modelled by perfect pinned conditions, i.e. all degrees of freedom set to zero, though they can lead to an artificial stiffening of the model [15]. The influence of the boundary conditions was investigated previously, using either clamped conditions for all the blank mesh nodes along the outer edges, or an applied pressure on the contact zones located in the clamping system [16]. It was found that the use of pressure condition leads to a lower and more realistic predicted force level than the one from the clamped conditions.

Finally, the choice of the mechanical model remains a topic of discussion. The influence of the hardening model, i.e., isotropic or mixed, has been discussed in the case of the SPIF process of an aluminum alloy 3003-O sheet of thickness 1.2 mm [17]. Results show a strong discrepancy between the predicted forces but the use of the mixed hardening model leads to a relevant decrease (up of 20%) in the FE simulation of a frustum cone with a wall angle of 50°. Such a conclusion is also presented in the case of AA5754-O sheets of thickness 1.5 mm [18], of magnesium alloy AZ31 sheet with a thickness of 1 mm [19], as well as an overestimation of the load with an isotropic hardening model for AA5182 sheets [20]. Henrard et al. [21] have also investigated the effect of different mechanical models (yield criterion, hardening type and hardening law) on the force prediction for the same material AA3003-O. The predicted loads depend strongly on the hardening law, rather than on the yield locus (isotropic von Mises and anisotropic Hill 1948 yield criteria). A similar conclusion is reached for a commercially pure titanium alloy sheet of thickness 0.5 mm [17]. Concerning the type of isotropic hardening law, a difference of 20% is observed between Voce and Swift laws on the predicted forces and the choice of the Voce law seems the most accurate one [21]. Moreover, the effect of a kinematic hardening contribution is less significant. Belchior et al. [13] have also studied the effect of the hardening laws, i.e. Ludwick and Voce ones, on the predicted forces to form a truncated cone made with AA5086-H111 with a thickness of 1 mm. A difference of 10% is noticed and the Voce law is selected such as the best suited hardening law to predict the forming loads. Though a clear conclusion is difficult to draw from the numerous previous studies, as different sheet thicknesses, ratio of reduction of the numerical model and materials are considered, it still comes out that an overestimation of the forming load in SPIF process is often observed. Hence, the selection of an accurate material model to predict the forming forces in SPIF process is not

an easy task. These difficulties mainly come from high plastic strain levels reached during the process (larger than 100%) and complex strain paths observed in this process [17]. For these reasons, the representation of the mechanical behavior should be appropriate.

The conventional tensile test is generally used to identify material parameters. Nevertheless, this kind of test is unable to reach high level of deformation or complex strain paths such as the ones obtained during SPIF process. Alternative solutions such as hydraulic bulge test or biaxial tensile tests extend significantly the strain range reached during the test, compared to uniaxial tension [22]. Then, it seems necessary to find the relevant material characterization tests for the SPIF process, taking into account the high level of deformation and the complex strain paths.

Several studies have presented the strain paths occurring during SPIF process. Experimental values of the strain components in the sheet plane were measured using Digital Image Correlation (DIC) technique [23], highlighting a zigzag strain path for a given material point, with a rather low but oscillating value of the minor strain and a major strain that can reach very high values. Such a cyclic path at a given material point arises from each pass of the moving tool, that generates bending and unbending with possible strain reversal [24]. Flores et al. [17] have investigated numerically the evolution of the strain path in a truncated cone, made of a mild steel sheet of thickness 0.8 mm, for one material point. They show that the oscillations occur when the tool is near the selected point and that the minor strain can have negative values. Abdelkefi et al. [14] have made a similar observation for the same shape but using a commercially pure titanium sheet of thickness 0.5 mm and they found out that the strain path evolves between compression, stretching and compression on the bottom surface of the sheet. Neto et al. [25] have also investigated the predicted strain paths in a conical part made of aluminium alloy 7075-O of thickness 1.63 mm. They observed that the strain paths are nearly under plane strain, which is consistent with the very low value of the minor strain. Based on the influence of strain path on the hardening of the material, there is therefore an interest to reproduce strain paths characteristics of the SPIF process for the material characterization.

Several kinds of complex strain paths including sequences of two-step and three-step linear strain paths have been investigated using different experimental set-ups [26]. However, it requires many experiments, which induce a high cost as well as the discontinuity of measurement of strain path due to the unloading. For these reasons, an alternative one-step procedure is to investigate the strain paths under biaxial tension [27-29]. In fact, this test shows

a great potential to reach high level of deformation and to follow non-linear strain paths, so it could be considered among the tests for material characterization [28].

It seems therefore that, to promote a better prediction of the forming loads, the mechanical model should be calibrated using strain paths representative of the SPIF process. In this study, the commercially pure titanium alloy T40 (grade 2) is considered for SPIF process applications, due to its biocompatibility, formability and corrosion resistance [30]. A limited number of studies has investigated the mechanical behavior of T40 sheets and mostly using tensile tests [31-34]. However, due to the highly anisotropic behavior of titanium alloys, other strain paths should be considered, e.g., hydraulic bulge test [35]. Within this context, the main aim of this study is to investigate the quality of the force prediction during SPIF process by using hydraulic bulge test data as input in the numerical model.

The present paper is organized in three parts. In section 2, the experimental procedure covering both the mechanical characterization of T40 alloy and the manufacturing of a truncated cone is presented. Uniaxial tensile tests at every 15° orientation with respect to the rolling direction and hydraulic bulge test are performed. The forming operation of the truncated cone is carried out with an instrumented CNC machine tool and the measured load components are output. A numerical reduced model of the SPIF process using two different hardening laws, either extracted from the tensile or bulge test data, is presented in section 3. The comparative study between FE predictions and experimental results in terms of the forming load and the part geometry is the subject of section 4.

2. Experimental procedures

2.1 Mechanical behavior of T40 alloy

2.1.1 Material

In the present study, the material is a commercially pure titanium alloy T40 (grade 2), provided as sheets, generally used for medical implants and aerospace applications. This material presents high biocompatibility, excellent formability and corrosion resistance. Moreover, this sheet material is often used for incremental forming process and forming applications [31-34]. T40 sheets are received as cold-rolled sheets with a nominal thickness of 0.5 mm. The chemical composition is given in Table 1. The equivalent grain size index is 10, corresponding to an average grain diameter of 11 μm (ISO643:2019).

Table 1

Chemical composition (in wt %) of the T40 alloy.

Fe	C	N	H	O_2	Ti
0.07	0.01	0.003	0.002	0.12	Bal.

2.1.2 Mechanical tests

Tensile and hydraulic bulge tests are performed to characterize the mechanical behavior. For all the tests, strains are computed with the DIC system Aramis, with one camera for the tensile tests and 2 cameras in stereo-correlation mode for the bulge tests. A total of 21 tensile tests are performed, with three tests every 15° from the rolling direction (RD) to the transverse direction (TD, at 90° to RD), to characterize both the anisotropy and the repeatability. Tensile tests are carried out with specimens of standard dog-bone geometry (ISO6892-1) of dimensions 75 x 12.5 mm^2 for the gauge area, at constant speed of 0.075 $mm.s^{-1}$, which induces an initial nominal strain rate of the order of 10^{-3} s^{-1}. The Cauchy stress component is calculated from the measured force assuming volume conservation and the logarithmic strain components are averaged over an area of length 40 mm. Table 2 presents the ultimate tensile strength and the initial yield stress (measured for a plastic strain of 0.02%) for each orientation.

Table 2

Mechanical properties of T40 sheets of thickness 0.5 mm. θ defines the angle to the rolling direction, R_m the ultimate tensile strength and σ_y the initial yield stress.

θ (°)	0	15	30	45	60	75	90
R_m (MPa)	327.7	331.1	315.7	292.9	306.9	321.4	318.5
σ_y (MPa)	207.5	200.0	219.1	234.2	248.4	260.0	265.7

A total of three circular specimens, of diameter 270 mm, is deformed by hydraulic bulging. A moving piston compresses a fixed volume of water, that applies an internal pressure P on the blank, which is clamped between a blank holder and a cylindrical die. The Cauchy stress component has been directly determined from the measured pressure using the following expression:

$$\sigma_b = \frac{P\,\rho}{2\,t} \quad (1)$$

with ρ the curvature radius at the pole and t the actual sheet thickness. The curvature radius ρ is calculated from the DIC measure, by fitting the outer deformed shape at the pole by a sphere and the water pressure is measured with a pressure sensor. The actual thickness is calculated from the strain components in the sheet plane and by assuming an isochoric transformation, in a small area centered around the apex. It should be highlighted that a very good repeatability is observed on the pressure vs equivalent strain, corresponding to raw data. Fig. 1 shows a deformed sample after a hydraulic bulging test up to rupture, as well as the major strain distribution recorded by DIC just before rupture. It highlights the large maximum equivalent strain reached during this test, of the order of 0.7.

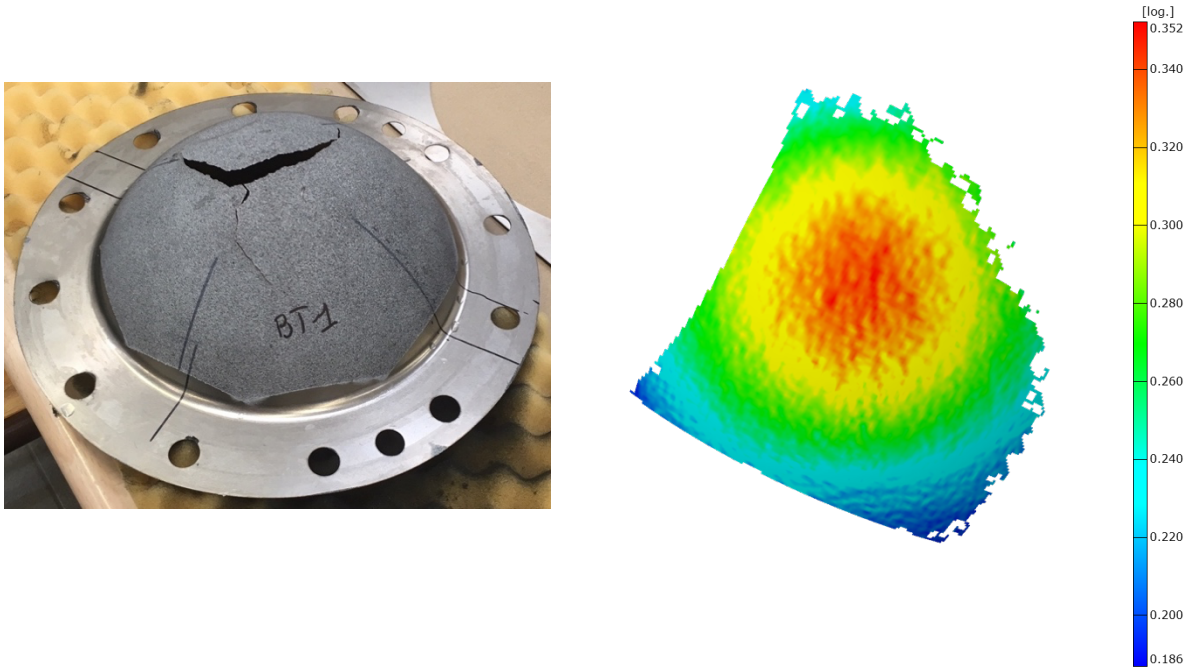

(a) (b)

Fig. 1 (a) Deformed specimen after hydraulic bulge test; the initial blank diameter is 270 mm (b) Major strain distribution captured by DIC just before rupture.

As shown in Fig. 2, the T40 sheet is a quite ductile material with elongation to fracture of over 0.4 for the tensile test in RD, while, for the bulge test, the equivalent plastic strain reaches a higher level of deformation, around 0.7. Moreover, the stress level obtained from the hydraulic bulge test is much higher than the one in tension and the hardening rate exhibits a non-monotonic evolution. Such characteristics have also been highlighted previously for a similar material [35, 36] and can be modeled with distortional hardening, via the evolution of the plastic

anisotropic coefficients with plastic strain. Moreover, the sigmoidal shape of the hardening curve noted during the bulge test has also been previously noted for CP titanium alloy, in uniaxial tension along different orientations to the rolling direction and a thicker material [37] and also in bulge test, for the same sheet thickness as in this study [35].

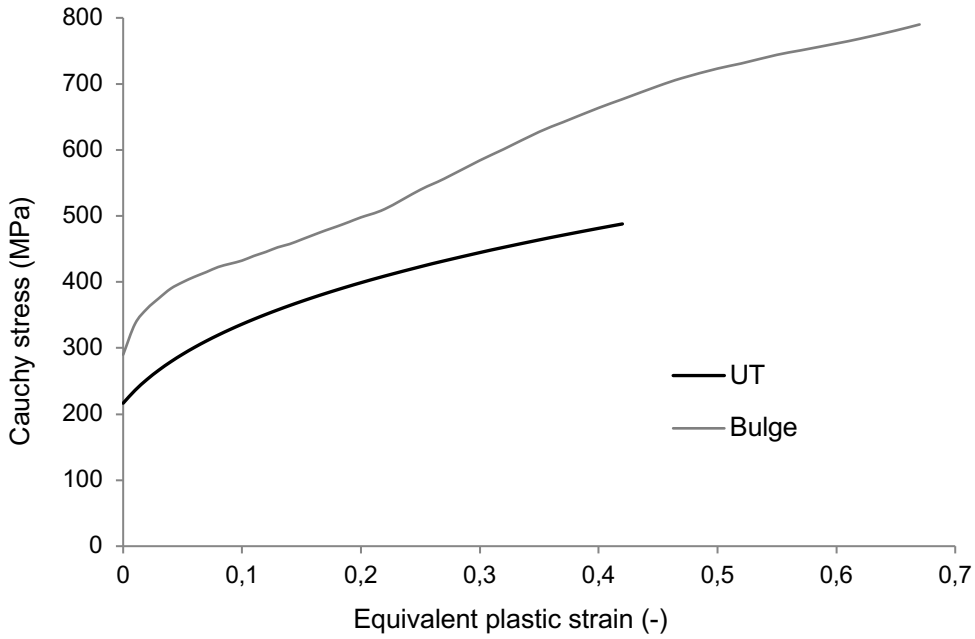

Fig. 2 Experimental hardening law of T40 output from uniaxial tensile (UT) tests and bulge tests. The equivalent plastic strain is calculated with von Mises yield criterion.

The initial yield stresses are presented for each orientation in Fig. 3. It can be noticed that the yield stress depends significantly on the material orientation, with a relative gap of 30% between the minimum and maximum values, reflecting the strong anisotropic behavior of T40 alloy. The plastic anisotropy coefficients r_θ for an orientation θ relative to the RD are calculated using Eq. 2 over the homogeneous deformation range.

$$r_\theta = \frac{d\,\varepsilon_{yy}^P}{d\,\varepsilon_{zz}^P} = \frac{d\,\varepsilon_{yy}^P}{-(d\,\varepsilon_{xx}^P + d\,\varepsilon_{yy}^P)} \quad (2)$$

where ε_{xx} and ε_{yy} are respectively, the longitudinal and transverse logarithmic strains measured by DIC. The deformation through thickness direction ε_{zz} is defined with the assumption of volume conservation. Exponent "p" stands for the plastic part of the strain component. Values of r_θ are listed in Table 3. The repeatability is evaluated by calculating half of the difference between the maximum and minimum values. It can be seen that the dispersion is rather small, with a maximum value of 3%.

Table 3

Plastic anisotropy coefficients r_θ for different angles to the rolling direction. The average value is given, as well as the dispersion, both calculated over 2-3 values for each direction.

θ (°)	0	15	30	45	60	75	90
r_θ	1.93 (±0.01)	1.75 (±0.02)	2.50 (±0.05)	4.49 (±0.02)	6.14 (±0.16)	6.31 (±0.14)	6.92 (±0.09)

As shown in Fig. 3, there is also a significant difference between the coefficients, which comforts the fact that T40 alloy exhibits a strong anisotropy. This finding is in agreement with observations reported in several studies for different sheet thicknesses [35, 37, 38]. It can be noticed then that there is a disparity of r_θ coefficient values, which could be explained by the difference of chemical composition and nominal thickness.

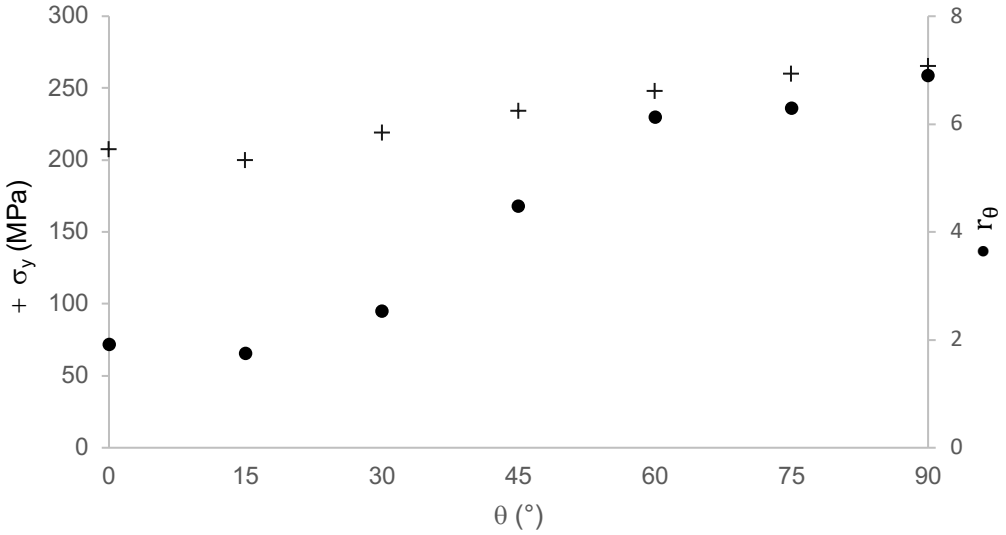

Fig. 3 Initial yield stress and plastic anisotropy coefficients at each 15° to the RD. Average values are plotted and the dispersion is given in Table 3.

2.2 Experimental SPIF process

A T40 square sheet of size 270 x 270 x 0.5 mm^3 is used to form a frustum cone of 45° wall angle (Fig. 4). The depth of the truncated cone is 29 mm. The forming tool is a hemispherical punch with a 15 mm diameter. The feed rate value of the tool is 360 mm/min and the tool rotation is locked. The SPIF operation is carried out on a three-axis CNC milling machine (Famup MCX600). The tool path consists of successive circular contours at constant Z, cf. Fig.

4 for the frame definition. The incremental step size value ΔZ is 1 mm per loop. The different points of the trajectory are calculated by a CAM (Computer-Aided Manufacturing) software. After each tool turn performed at constant Z, the tool shifts radially, which causes a loss of contact with the sheet metal before descending along Z and resuming a circular path at constant Z. The radial offset is not constant, the path is defined in order to respect a maximum axial or radial offset of 1 mm between each turn at a constant Z. This maximum pitch value of 1 mm makes it possible to obtain a satisfactory surface finish of the formed part while maintaining acceptable forming times. The forming force components are measured by a six-axes force/torque sensor ATI Omega190. During the forming operation, the rolling direction of the sheet corresponds to the X axis defined in Fig. 4. The clamping system (Fig. 4b) is composed of a blank holder screwed on a rigid frame. The contact between tool and sheet is lubricated to minimize the friction. The duration of the forming operation is about 30 min.

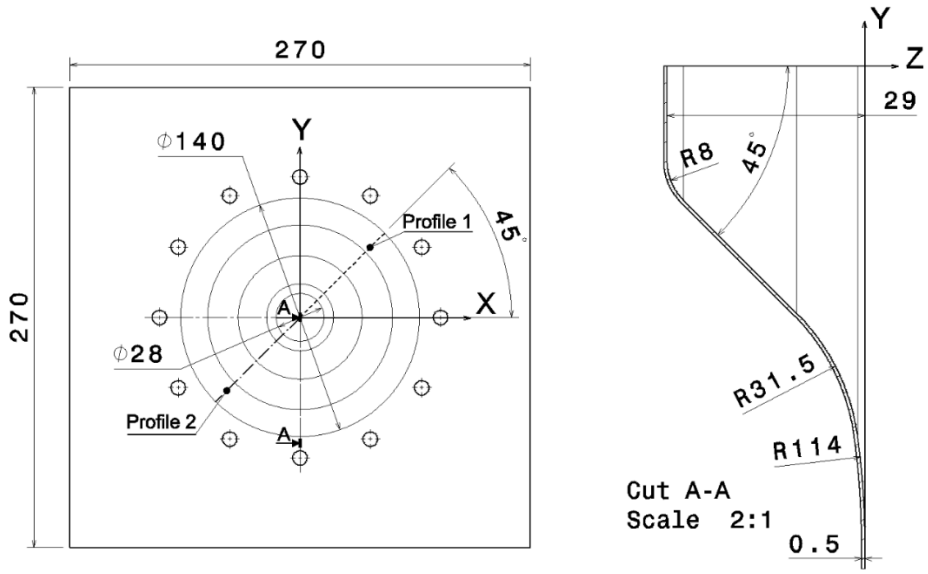

(a) Dimensions (in mm) of 45° wall angle truncated cone

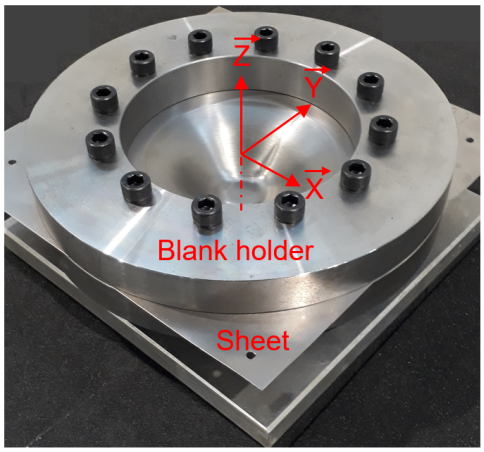

(b) Truncated cone shape formed in experiment

Fig. 4 Part geometry and experimental setup for the SPIF process

- **Force measurement**

Figure 5 presents the forming force component F_Z measured in the axial direction as a function of the tool displacement U_z. At the end of each circular path at constant Z, the imposed tool path leads to a loss of contact between the tool and the sheet metal, due to the radial inward movement of the tool, which results in a return of the force F_Z down to zero. At each new Z-increment, the tool-to-sheet contact restoration generates a force peak, especially for the deepest passes. As shown on the detailed view of Fig. 5, for a circular path at Z = 26 mm, the force F_Z then stabilizes quickly from the beginning of the considered path and is relatively constant over one revolution. The same tendencies have been observed in previous works [1, 17, 18, 20, 21]. The axial load F_Z increases gradually during successive increments of the tool position along Z. The maximum value of axial load is about 910 N and remains stable until the end of forming.

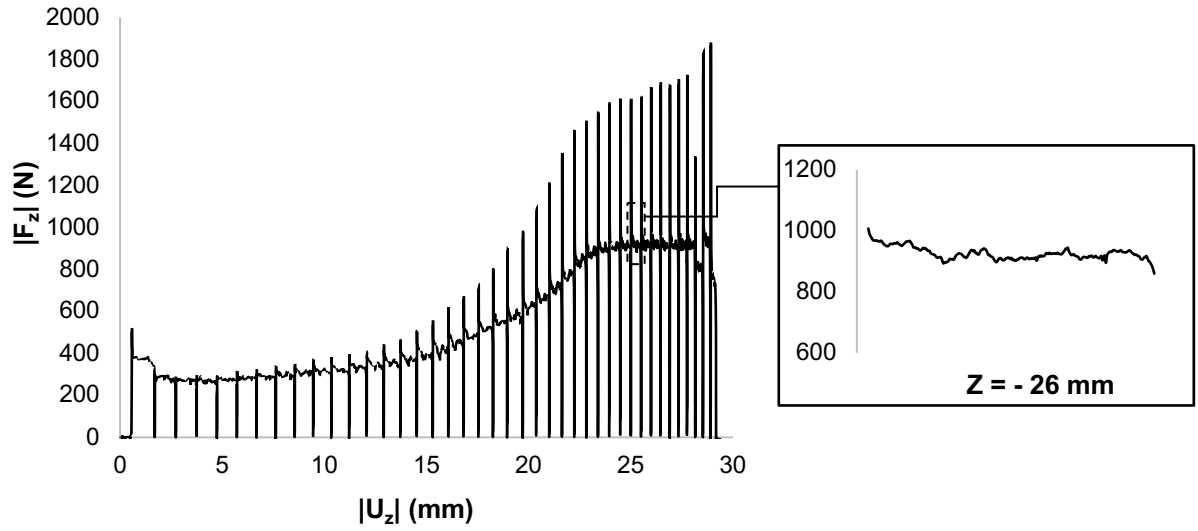

(a) for the complete forming phase (b) for a given Z-position

Fig. 5 Forming force component measured along the Z-axis. As the load component F_z and tool displacement along z, U_z, have negative values, the absolute value is used out of clarity's reasons.

- **Profile and thickness measurement**

At the end of the SPIF operation, before the unclamping stage, the final shape of the formed truncated cone is measured by a 3D scan machine. The part still clamped between the blankholder and the rigid frame is disengaged from the forming area, for a better accessibility. The assembly is then turned by 90° so that the Z axis becomes horizontal, which allows access to both faces in a single measurement operation of the scanner. The two faces of the part, bottom and top (the upper side corresponds to the tool side), are scanned in order to evaluate the final blank thickness. The accuracy of the scan machine is ± 0.015 mm. In Figs. 6 and 7, measurements are given for a cutting plane located at 45° to the XZ plane (cf. Fig. 4a). In these figures, the experimental measurements according to the two profiles "Profile 1" and "Profile 2" defined in Fig. 4a are superimposed. As can be seen by comparing the results in Fig. 6, very few differences are observed between profiles 1 and 2, either for the lower or upper side of the part. The final shape and the thickness evolution can be divided into 3 areas: AB, BC, and CD. In AB region, the blank shows a small deformation, therefore the thickness is close to its initial value. In BC region, the thickness swiftly reduces and then recovers its initial value in CD region.

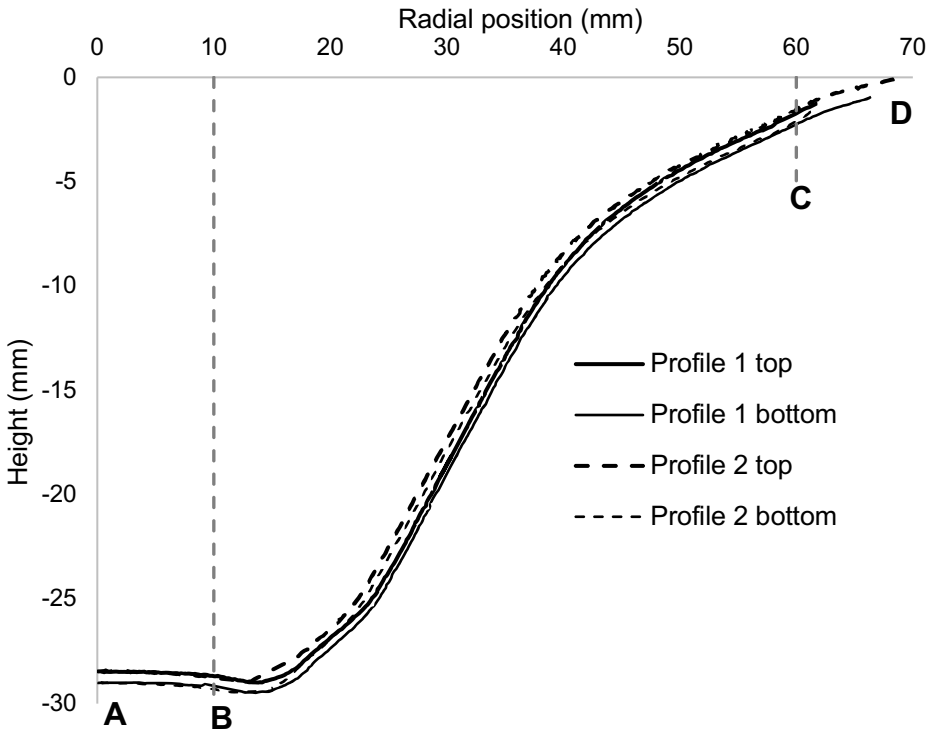

Fig. 6 Experiments: geometry of the final shape along profiles at 45° to RD, measured on the bottom and top (tool side) surfaces

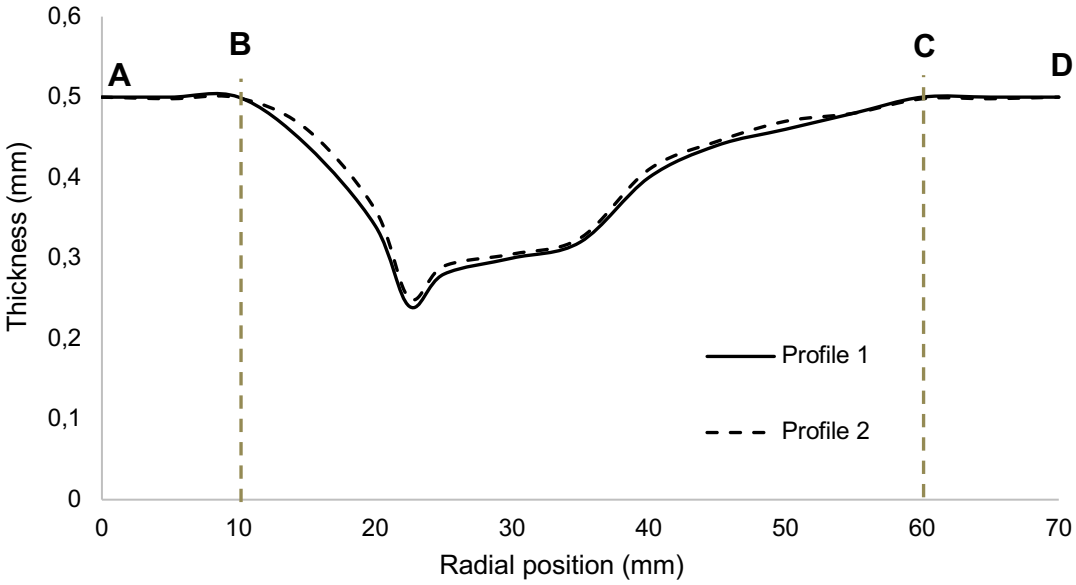

Fig. 7 Experiments: thickness distribution along two profiles at 45° to RD

3. Numerical model

The simulation of the truncated cone is performed with Abaqus software, using an implicit formulation. As discussed before, one fourth of the sheet is considered to reduce the computation time (Fig. 8). Two types of elements, S4R and C3D8I, are considered. The S4R element is a 4-node shell element with reduced integration and a large-strain formulation. The C3D8I element is a 8-node linear brick element with full integration and incompatible modes. Four layers of elements are used in the sheet thickness, to take account of the through thickness shear. The X-axis still corresponds to the rolling direction of the sheet. The X and Y-axes are also the symmetry axes of the reduced model. The hemispherical punch is modeled as a rigid body. The same Z level strategy for the tool displacement as the one described in the experimental section is applied. As discussed before, the modeling of the clamping system affects the prediction of the forming loads. Embedding condition is applied along the outer circular edge. This boundary condition tends to rigidify the mounting system and then leads to an overestimation of the forming loads. Modeling the clamping pressure can lead to more realistic results but the knowledge of pressure value and contact conditions is not self-evident. Lubrication is used during the forming of the cone, so frictionless contact is considered between the tool and the sheet.

The elastic behavior of the material is defined by Young's modulus (110 GPa) and Poisson's ratio (0.3). Two different hardening laws are implemented in the simulation. They are directly introduced in Abaqus from the uniaxial tensile (UT) tests and bulge tests (Fig. 2). The influence of the modeling of anisotropy on the results will be discussed by comparing the results from the isotropic von Mises yield criterion and the anisotropic Hill48 yield criterion. The parameters of the Hill48 yield criterion (Table 4) are identified from the uniaxial tensile tests, using the plastic anisotropy coefficients.

Table 4

Parameters of the Hill 48 anisotropic yield criterion, calculated from the plastic anisotropy coefficients r_0, r_{45} and r_{90} (G+H=1).

F	G	H	N	L	M
0.096	0.34	0.66	2.17	1.5	1.5

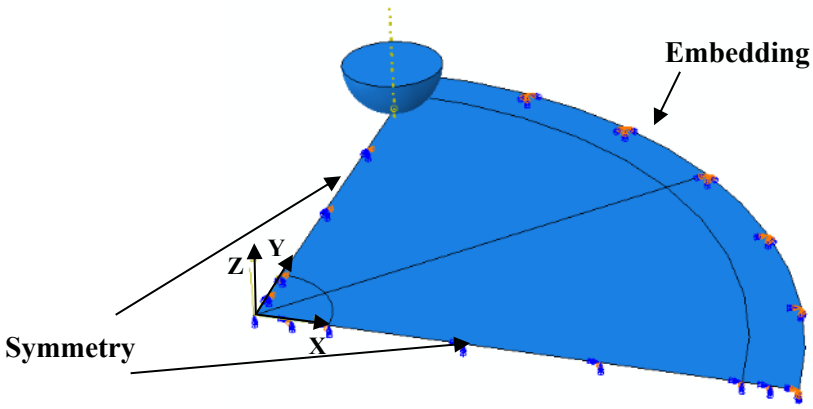

Fig. 8 FE model and boundary conditions applied to one fourth of the blank.

Finally, in order to quantify the influence of material characterization and modeling of the sheet material behavior, the results of five numerical simulations are compared with the experimental results. Four simulations are based on the von Mises yield criterion (UT Shell, UT 3D, Bulge Shell and Bulge 3D), the fifth (UT 3D Hill48) on the Hill48 yield criterion.

4. Results and discussion

This discussion is subdivided in 4 main parts, dealing with the influence of the finite element type on the load prediction, the influence of hardening law on the predicted load and part geometry, the analysis of the strain paths occurring in SPIF process and finally, suggesting some recommendations on the proper choices to represent the mechanical behavior of the material in the FE model, involving hardening and initial anisotropy.

4.1 Influence of the finite element type on the load prediction

Figure 9 shows a comparison of experimental and predicted vertical load components. It should be emphasized that the peaks shown in Fig. 5 are removed and the average of the vertical force over one cycle, at a constant Z value, is calculated and used in the comparison between experiments and simulation. For both hardening law, 3D and shell model predictions are compared. It can be seen that the 3D model vertical load prediction is always higher than the shell model one, by approximately 7% above a tool displacement of 5 mm. Moreover, the gap decreases significantly when reaching the load stagnation at a displacement around 15-17 mm. Such a small difference may come from the rather thin sheet used in this study, of 0.5 mm thickness, leading to a rather weak influence of the through thickness stress components on the global load.

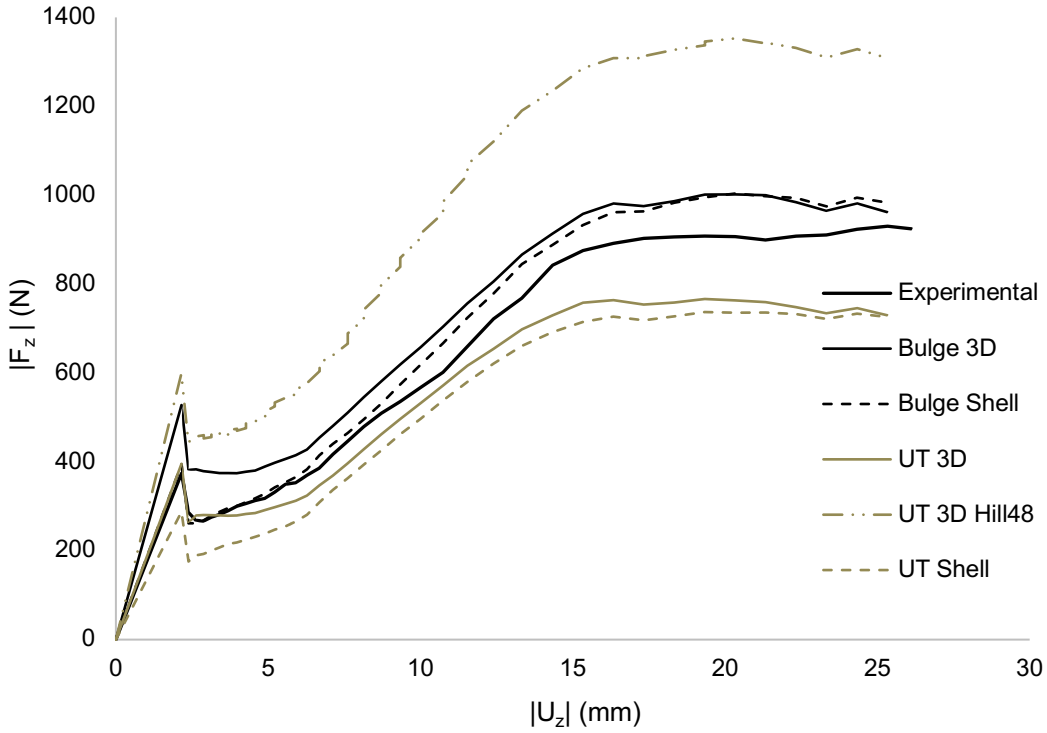

Fig. 9 Comparison of experimental and predicted vertical forming loads. As the load component F_z and tool displacement along z, U_z, have negative values, the absolute value is used out of clarity's reasons.

4.2 Influence of the hardening law on the predicted load and part geometry

In this part, the numerical and experimental results for the forming load, final part geometry and thickness distribution are compared. As shown in Fig. 9, the force reaches a steady maximum value after a Z-displacement of about 15 mm. The FE simulations with material behavior from tensile tests noticeably underestimate the steady value of the forming load, with a relative gap of 18-20%, except when using Hill48 yield criterion, for which a large overestimation is noticed. The use of Hill48 yield criterion leads to an overestimation of the stress level in biaxial tension, as shown in a previous study for a similar material [36], that could explain the large overestimation of the forming load. Nevertheless, for the simulations with the bulge material characterization, a difference of 7% is noticed between the experimental force and numerical values. Such a difference in the hardening curve level could be well captured by a relevant anisotropic yield criterion [35,36]. However, for a rapid design, the hardening curve extracted from a bulge test associated to an isotropic yield criterion, is a very interesting choice to model the mechanical behavior of CP titanium alloy.

Figure 10 presents the comparative study between the experimental and numerical results of the deformed part geometry, before the unclamping stage. The final shape after unclamping or springback is not considered at this stage, as the mechanical model is based solely on isotropic hardening with a constant Young's modulus. In the simulation, the part profile is taken from the median plane of the model shown in Fig. 8, which corresponds to a 45° cutting plane of the XZ plane. For the formed part, the measured profile corresponds to the bottom side of the sheet metal (on the opposite side to the tool with respect to the sheet). As shown in Fig. 10, FE simulations predict well the wall region and underestimate the cone bottom. As explained in previous studies [39-40], the constitutive model does not seem to be a key factor to predict accurately the deformed shape before springback, but the use of a reduced or full numerical model seems to be more influent [6]. Hence, it can be highlighted that the prediction of the final shape is insensitive to the finite element type (shell or 3D) or hardening laws (tensile or bulge). Differences observed in Fig. 10 can be explained by the modeling adopted here, i.e., only one fourth of the blank is modeled and symmetry conditions are applied on X and Y-axes.

Additionally, the predicted and experimental thickness of the deformed part at the final stage are displayed in Fig. 11. The thickness distribution is represented along only the quarter of the model due to the symmetry conditions used in FE simulations. Both experimental and numerical curves reveal a maximal thinning at the same location, for a radial position around 22.5 mm. It is found that, when using a 3D model, the numerical thickness distribution in the radial direction is generally in accordance with the experimental curve, despite a small acceptable discrepancy. Meanwhile, the shell model overestimates the thickness distribution and presents a mismatch with the experimental curve at the bottom radius. The shell element model does not permit a good representation of the transverse shear deformation, which may not be negligible [20]. In addition, the use of bulge or tensile hardening laws has no effect on the thickness distribution. From the above results, it can be concluded that the thickness distribution depends on the element type (shell or 3D) and that the thickness distribution is rather insensitive to the hardening law, as characterized in uniaxial or biaxial tension.

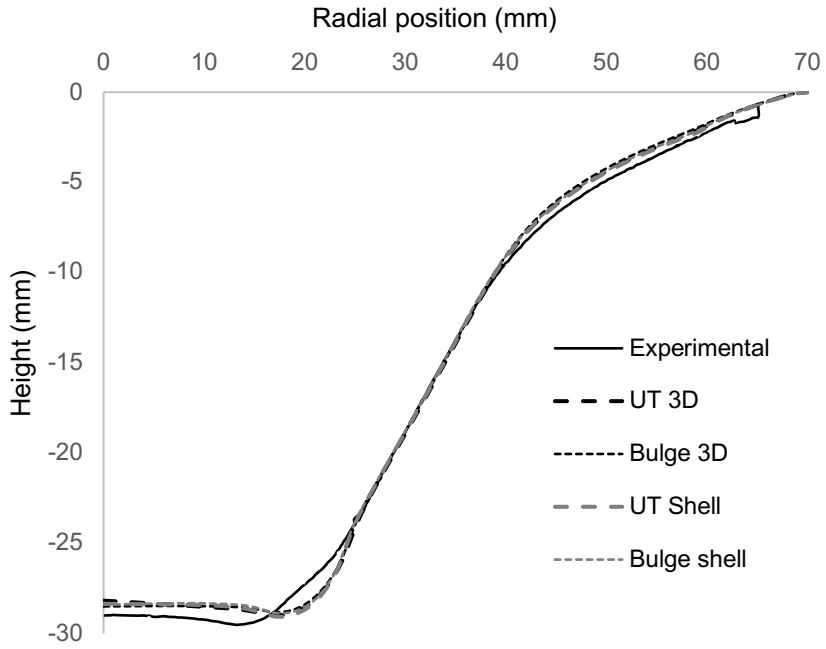

Fig. 10 Comparison of the final shape geometry, before springback

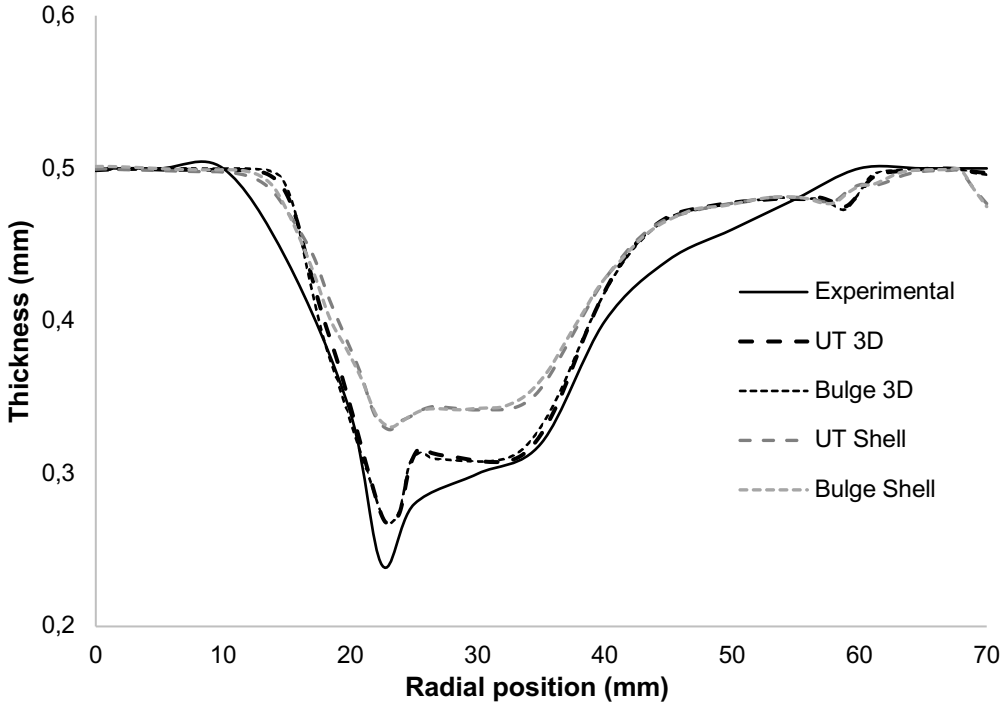

Fig. 11 Comparison of the thickness distribution

4.3 Influence of the strain path on the mechanical behavior

The influence of the mechanical behavior, either tested in uniaxial tension or bulge test, is certainly related to the local strain paths occurring during the forming process. The strain

history as a function of the tool position is analyzed for one of the previous models due to the similarity of the predictions [11]; out of simplicity's reasons, the shell element model is used. The evolution of the strain path, corresponding to the evolution of the major strain versus minor strain in the sheet plane at the point P_1 (Fig. 12) situated on the outer surface of the sheet is presented in Fig. 12(a) for the 30 cycles of the forming process. The selected point is defined initially on the undeformed mesh at a distance corresponding to half of the initial radius.

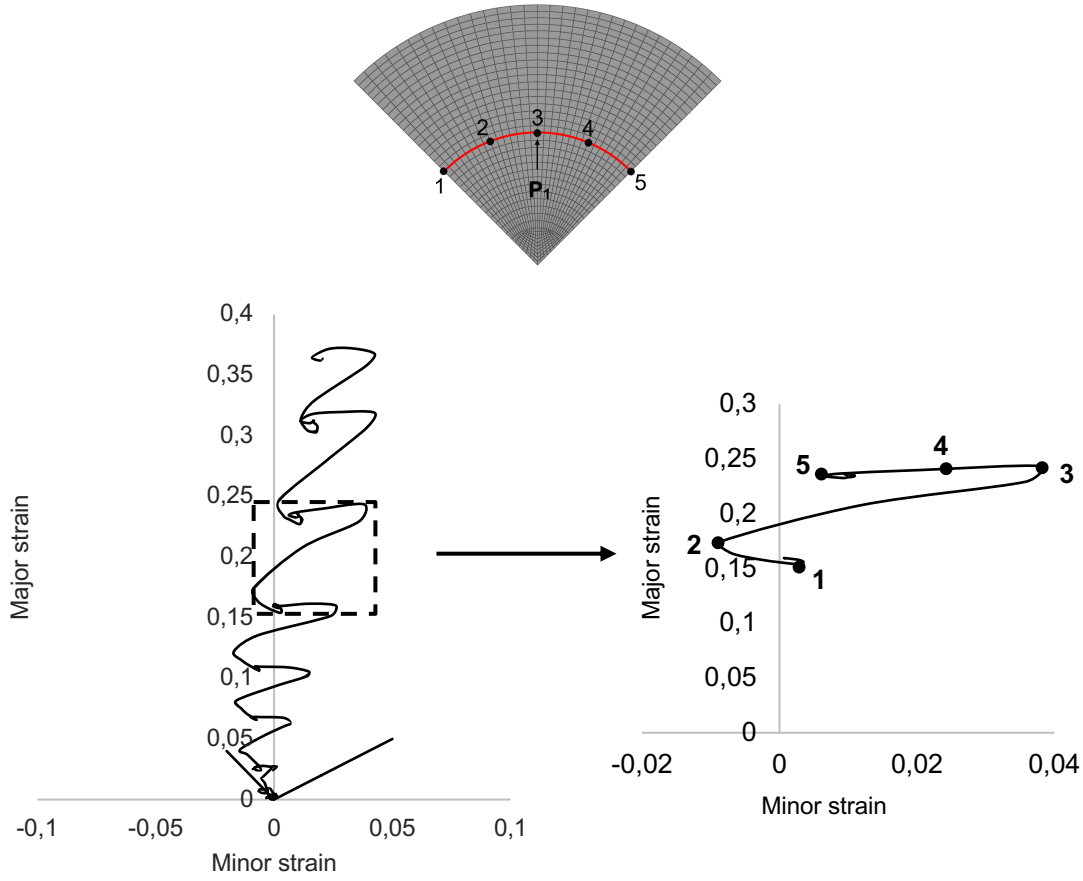

(a) For the whole forming stage (b) For the 28th forming cycle

Fig. 12 Evolution of the strain path at point P_1 located on the lower face of the formed part (opposite side to the tool), and represented on the mesh at the top. Note that the scale on the minor strain axis is much lower than the one on the major strain axis. (a) The information for the whole process is plotted. The 2 straight lines represent respectively the biaxial state (on the right-hand side) and the uniaxial state (on the left-hand side). (b) Magnified view for only one cycle (28th) corresponding to a given Z-position.

A cyclic feature due to the successive pattern of the tool path is observed. The strain path at the point P_1 for the 28^{th} cycle is presented in Fig. 12(b). The numbers 1 to 5 stand for five specific positions of the tool: from the position 1 to 2, the major strain does not evolve significantly while the minor strain decreases and reaches negative values. When the tool moves from position 2 to position 3, a relevant change in the strain path is noticed, which corresponds to the beginning of the contact between the tool and the selected point. The sheet is subject there to a quasi-equibiaxial stretching and reaches the maximum of major strain at position 3. From the position 3 of the tool, a new strain path change occurs, as the tool moves far from point P_1, with a decrease of the minor strain in the circumferential direction and a nearly constant major strain, in the radial direction. As shown in Fig. 12, the strain path is nearly under plane strain, and this observation is in good agreement with previous studies [26]. Therefore, it comes out that a major strain increase, from around 0.16 up to 0.24, occurs in a nearly biaxial strain state mode and this phenomenon occurs repeatedly, as evidenced in Fig. 12(a). The choice of the hardening law derived directly from a biaxial strain state (bulge test) to represent the material behavior during the SPIF process is in very good agreement with the local strain path.

Moreover, the influence of the boundary conditions of the FE model should be recalled here. Indeed, as discussed in section 1, preventing any radial displacement under the clamping system, by using embedded conditions, tends to introduce a certain artificial stiffness, leading to a load increase. Such a phenomenon can be avoided by using a pressure distribution. However, it demands additional information from the experiments, to calibrate accurately the extra parameters, that was not available in this study. A more realistic model of the clamping system would lead to a load decrease, thus decreasing further the gap between the predicted load, when using the hardening curve from the bulge test, and the experimental value. The same trend would be observed for the predicted load corresponding to the hardening curve coming from the tensile test, leading to an increased discrepancy between experiments and the numerical prediction.

4.4 Taking account of the anisotropic yield. A practical approach

It was previously stated in section 4.2 that the highly different levels recorded for the hardening curve, i.e., the evolution of the equivalent plastic strain with the equivalent stress, in uniaxial

tension and biaxial tension (coming from a bulge test in this study) can be taken into account by considering anisotropic yield criteria. Such a trend is certainly the most accurate one, but at the same time, the most demanding one in terms of the number of mechanical tests and the model calibration effort. In this study, Hill48 anisotropic yield criterion is also used with the hardening curve derived from tension and with a calibration based on the plastic anisotropic ratios, cf. Tables 3 and 4. It can be seen in Fig. 9 that the corresponding predicted load is much higher than all the others, including the experimental one, leading to the conclusion that the combination of von Mises yield criterion coupled with the hardening curve obtained in biaxial tension, as it is an important strain path in SPIF, gives a rather accurate load prediction. It represents a good compromise between material characterization and reliability of the vertical load.

5. Conclusions

In the present paper, a SPIF process is investigated both from experimental and numerical standpoints. Mechanical characterization is done by tensile tests in directions at each 15° from the rolling direction and hydraulic bulge test, to identify material parameters of a commercially pure T40 alloy. FE simulations of the SPIF process of a truncated cone are performed using hardening laws either derived from uniaxial or biaxial tensile states and two finite element types (shell and 3D). Influence of the calibrated models on the predicted vertical loads, strain path, final shape and thickness distribution is discussed. The following insights can be drawn:

- The hardening law derived directly from the bulge test data, and associated with von Mises yield criterion, seems to be the most suitable one to predict the forming forces with a small gap of 7%. This result should be put in parallel to the contribution of the biaxial state to the strain path during the SPIF process.
- The prediction of the forming loads depends more strongly on the hardening law than on the finite element type (shell or 3D).
- The global strain path in SPIF corresponds to plane strain conditions, with small minor strain values and more importantly, changes locally from uniaxial tension, plane strain tension and biaxial tension strain state.
- The final shape and thickness depend on the hardening law and on the finite element type, especially in the corner radius at the bottom of the cone.

Compliance with ethical standards

Conflict of interest: The authors declare that they have no conflict of interest.

Acknowledgments: the authors are indebted to the Région Bretagne for the financial support via grant SAD17027-Ti4FI.

References

1. Belchior J, Leotoing L, Guines D, Courteille E, and Maurine P (2014) A process/machine coupling approach: application to robotized incremental sheet forming. J. Mater. Process. Technol. 214(8): 1605-1616. https://doi.org/10.1016/j.jmatprotec.2014.03.005
2. Belchior J, Guillo M, Courteille E, Maurine P, Léotoing L, Guines D (2013) Off-line compensation of the tool path deviations on robotic machining: application to incremental sheet forming. Robotics and Computer-Integrated Manufacturing, 29: 58-69. http://dx.doi.org/10.1016/j.rcim.2012.10.008
3. Ambrogio G, Costantino I, De Napoli L, Filice L, Fratini L, and Muzzupappa M (2004) Influence of some relevant process parameters on the dimensional accuracy in incremental forming: a numerical and experimental investigation. J Mater Process Technol 154: 501–507. http://dx.doi.org/10.1016/j.jmatprotec.2004.04.139
4. Han F, MO J, Qi H (2013) Springback prediction for incremental sheet forming based on FEM-PSONN technology. Trans Nonferrous Met Soc China, 23:1061– 1071. https://doi.org/10.1016/S1003-6326(13)62567-4
5. Duflou J, Habraken AM, Cao J, Malhotra R, Bambach M, Adams D, Vanhove H, Mohammadi A, Jeswiet J (2018) Single point incremental forming: state-of-the-art and prospects. Int J Mater Forming 11: 743-773. https://doi.org/10.1007/s12289-017-1387-y
6. Henrard C (2008) Numerical Simulations of the Single Point Incremental Forming Process, PhD thesis, Université de Liège, Belgium.
7. Emmens W C, Van Den Boogard A V (2009) An overview of stabilizing deformation mechanisms in incremental sheet forming. J Mater Process Technol, 209: 3688–3695. https://doi.org/10.1016/j.jmatprotec.2008.10.003
8. Yamashita M, Gotoh M, Atsumi SY (2008) Numerical simulation of incremental forming of sheet metal. J Mater Process Technol, 199: 163–172. https://doi.org/10.1016/j.jmatprotec.2007.07.037

9. Fratini L, Ambrogio G, Di Lorenzo R, Filice L, Micari F (2005) Three-dimensional FE simulation of single point incremental forming: experimental evidences and process design improving. VIII International Conference on Computational Plasticity, Complas VIII, Barcelona.
10. Ceretti E, Giardini C, Attanasio A (2004) Experimental and simulative results in sheet incremental forming on CNC machines. J Mater Process Technol, 152:176–184. https://doi.org/10.1016/j.jmatprotec.2004.03.024
11. Hadoush A, Van Den Boogard A H (2009) Substructuring in the implicit simulation of single point incremental forming. Int J Mater Form, 2: 181–189. https://doi.org/10.1007/s12289-009-0402-3
12. Sena J I V, De Sousa R A, Valente RAF (2010) Single point incremental forming simulation with an enhanced assumed strain solid-shell finite element formulation. Int J Mater Form, 3: 963-966. https://doi.org/10.1007/s12289-010-0929-3
13. Belchior J, Leotoing L, Guines D, Ragneau E (2013) Force prediction for correction of robot tool path in single point incremental forming. Key Eng Mater, 554:1282-1289. https://doi.org/10.4028/www.scientific.net/KEM.554-557.1282
14. Abdelkefi A, Guines D, Léotoing L, Thuillier S (2019) Influence of the mechanical model of titanium T40 on the predicted forces during incremental forming process. AIP Conference Proceedings, 2113: 170010. https://doi.org/10.1063/1.5112726
15. Bouffioux C, Henrard C, Gu J, Duflou J, Habraken A M, and Sol H (2007) Development of an inverse method for identification of materials parameters in the single point incremental forming process. IDDRG.
16. Belchior J (2013) Développement d'une approche couplée matériau/structure machine: application au formage incrémental robotisé, PhD thesis, INSA Rennes.
17. Flores P, Duchene L, Bouffioux C, Lelotte T, Henrard C, Pernin N, and Habraken A M (2007) Model identification and FE simulations: effect of different yield loci and hardening laws in sheet forming. Int J Plast 23: 420-449. https://doi.org/10.1016/j.ijplas.2006.05.006
18. Said L B, Mars J, Wali M, Dammak F (2017) Numerical prediction of the ductile damage in single point incremental forming process . Inter J Mech Sci, 131: 546-558. https://doi.org/10.1016/j.ijmecsci.2017.08.026
19. Duc-Toan N, Jin-Gee P, Young-Suk K (2010) Combined kinematic/isotropic hardening behavior study for magnesium alloy sheets to predict ductile fracture of rotational

incremental forming. Int J Mater Form, 3: 939-942. https://doi.org/10.1007/s12289-010-0923-9

20. Benedetti M, Fontanari V, Monelli B, Tassan B (2017) Single-point incremental forming of sheet metals: Experimental study and numerical simulation. Proceedings of the Institution of Mechanical Engineers. J Eng Manuf, 231: 301-312. https://doi.org/10.1177/0954405415612351
21. Henrard C, Bouffioux C, Eyckens P, Sol H, Duflou, J R, Van Houtte P, and Habraken A M (2011) Forming forces in single point incremental forming: prediction by finite element simulations, validation and sensitivity. Comput. Mech 47: 573-590. https://doi.org/10.1007/s00466-010-0563-4
22. Liu W, Guines D, Leotoing L, and Ragneau E (2016) Identification of strain rate-dependent mechanical behaviour of DP600 under in-plane biaxial loadings. MAT SCI ENG- A, 676: 366-376. https://doi.org/10.1016/j.msea.2016.08.125
23. Eyckens P, Belkassem B, Henrard C, Gu J, Sol H, Habraken AM, Van Houtte P (2011) Strain evolution in the single point incremental forming process: digital image correlation measurement and finite element prediction. Inter J Mater Form, 4: 55-71. https://doi.org/10.1007/s12289-010-0995-6
24. Emmens W C, Van Den Boogaard AH (2009) An overview of stabilizing deformation mechanisms in incremental sheet forming. J Mater Process Technol 209: 3688-3695. https://doi.org/10.1016/j.jmatprotec.2008.10.003
25. Neto D M, Martins J M P, Oliveira M C, Menezes L F, and Alves J L (2016) Evaluation of strain and stress states in the single point incremental forming process. Int J Advan Manuf Techn, 85(1-4):521-534. https://doi.org/10.1007/s00170-015-7954-9
26. Butuc M, Barlat F, Gracio J, Vincze G (2013) A theoretical study of the effect of the double strain path change on the forming limits of metal sheet. Key Eng Mater 554: 127-138. https://doi.org/10.4028/www.scientific.net/KEM.554-557.127
27. Zhang S, Leotoing L, Guines D, Thuillier S, Zang S L (2014) Calibration of anisotropic yield criterion with conventional tests or biaxial test. Int. J. Mech. Sci 85: 142-151. https://doi.org/10.1016/j.ijmecsci.2014.05.020
28. Leotoing L, and Guines D (2015) Investigations of the effect of strain path changes on forming limit curves using an in-plane biaxial tensile test. Int. J. Mech. Sci, 99: 21-28. https://doi.org/10.1016/j.ijmecsci.2015.05.007
29. Song X (2018) Identification of forming limits of sheet metals with an in-plane biaxial tensile test, PhD thesis, INSA Rennes.

30. Bannon B P, Mild E E (1983) Titanium Alloys for Biomaterial Application: An Overview, Titanium Alloys in Surgical Implants. A Symposium ASTM STP, 796 : 7-16. https://doi.org/10.1520/STP28931S
31. Saidi B, Laurence G, Boulila M, Cherouat A, and Nasri R (2016) Etude expérimentale et numérique des efforts lors du formage incrémental de tôles en titane. JET 2016, Hammamet, Tunisie.
32. Sakhtemanian M R, Honarpisheh M, Amini S (2018) Numerical and experimental study on the layer arrangement in the incremental forming process of explosive-welded low-carbon steel/CP-titanium bimetal sheet. Int J Adv Manuf Techn, 95: 3781-3796. https://doi.org/10.1007/s00170-017-1462-z
33. Araújo R, Teixeira P, Silva M, Reis A, Martins PA (2013) Single point incremental forming of a medical implant. Key Eng Mater, 554: 1388-1393.DOI:104028/www.scientific.net/kem.554-557.1388
34. Araújo R, Teixeira P, Montanari L, Reis A, Silva MB, Martins P A (2014) Single point incremental forming of a facial implant. Prosthetics and orthotics international, 38: 369-378. https://doi.org/10.1177/0309364613502071
35. Pham Q T, Lee M G, Kim Y S (2019) Characterization of the isotropic-distortional hardening model and its application to commercially pure titanium sheets. Int J Mech Sci, 160: 90-102. https://doi.org/10.1016/j.ijmecsci.2019.06.023
36. Ishiki M, Kuwabara T, Hayashida Y (2011) Measurement and analysis of differential work hardening behavior of pure titanium sheet using spline function. Int. J. Mater. Forming 4:193-204. https://doi.10.1007/s12289-010-1024-5
37. Baral M, Hama T, Knudsen E, Korkolis Y P (2018) Plastic deformation of commercially-pure titanium: experiments and modeling. Int. J. Plas., 105:164-194. https://doi.org/10.1016/j.ijplas.2018.02.009
38. Bathini U (2010) A Study of Microstructure, Tensile Deformation, Cyclic Fatigue and Final Fracture Behavior of Commercially Pure Titanium and a Titanium Alloy. PhD thesis. https://etd.ohiolink.edu/
39. Revil-Baudard B (2010) Simulation du comportement mécanique des alliages de titane pour les procédés de mise en forme à froid. PhD thesis, Mines ParisTech (in French).
40. Hannon A, Tiernan P (2008) A review of planar biaxial tensile test systems for sheet metal. J mater process technol, 198: 1-13. https://doi.org/10.1016/j.jmatprotec.2007.10.015